Chapter 3
Surface-Sensitive X-ray Diffraction Across the Pressure Gap

Andreas Stierle, Johan Gustafson and Edvin Lundgren

Abstract In this chapter surface-sensitive X-ray diffraction is introduced as an important crystallographic tool for the investigation of surfaces and nanostructures under high pressure reaction conditions and elevated temperatures which are relevant for industrial catalysis. After the introduction surface-sensitive X-ray diffraction methods are briefly explained and specialized instrumentation developed for the in situ investigation of surfaces and nanostructures across the pressure gap is presented combined with simultaneous measurement of the concentrations of reactants and products. In the following an overview of the experimental results is given: First the (near)- ambient pressure oxidation of 3d, 4d, and 5d transition metals is discussed which are relevant for oxidation catalysis. Afterwards catalytic reaction experiments in batch mode are reported, followed by an overview of current research using a flow reactor for surface-sensitive X-ray diffraction. Finally a perspective is given for future research directions.

3.1 Introduction

Surface-sensitive X-ray diffraction methods were introduced as a surface characterization tool in the mid-eighties of the last century, when hard X-ray synchrotron light from large particle accelerators became available for solid state physicists [1–3]. The method portfolio comprises surface X-ray diffraction (SXRD), grazing incidence X-ray diffraction (GIXRD), X-ray reflectometry (XRR), and grazing incidence small angle X-ray scattering (GISAXS). Since then, the methods became standard tools for the analysis of surface, interface and thin film structures. The

A. Stierle (✉)
Deutsches Elektronen Synchrotron DESY, Hamburg, Germany
e-mail: andreas.stierle@desy.de

J. Gustafson · E. Lundgren
Lund University, Lund, Sweden
e-mail: johan.gustafson@sljus.lu.se

E. Lundgren
e-mail: edvin.lundgren@sljus.lu.se

J. Frenken and I. Groot (eds.), Operando *Research in Heterogeneous Catalysis*,
Springer Series in Chemical Physics 114, DOI 10.1007/978-3-319-44439-0_3

main advantage of hard X-ray-based surface-sensitive diffraction techniques (photon energy 10–100 keV), as compared to electron-based surface characterization tools, is that they can be routinely applied in situ, under any type of surrounding environment at variable temperatures, especially during realistic gas pressures and compositions relevant for heterogeneous catalysis. In addition, the X-ray diffraction experiments are not hampered by insulating sample charging effects. Surface-sensitive X-ray diffraction methods are especially suited for the investigation of catalytic reactions, since they allow addressing the atomic structure of catalyst surfaces, which gives important insight into reaction mechanisms. This deeper level of fundamental insight into the surface structure of a working catalyst, as compared to X-ray powder diffraction or extended X-ray absorption fine structure (EXAFS) experiments, however, sets constraints on the sample itself: For all surface-sensitive X-ray diffraction methods a planar surface geometry is required; for crystallographic information single-crystal surfaces, epitaxial nanoparticles or nanostructures are mandatory. The wide range of temperatures and gas pressures accessible by surface-sensitive X-ray diffraction allows a direct comparison of the experimental results with theoretical calculations by *ab initio* density functional theory coupled to thermodynamics, as presented in Chap. 7 of this book.

This chapter is organized as follows: In the first part the concept of surface-sensitive X-ray diffraction methods is briefly introduced and novel sample environments for in situ experiments are described. In the second part, near-atmospheric pressure oxidation experiments of 4d and 5d metal surfaces and nanoparticles are discussed. The oxide phases are considered to be relevant as active phases for oxidation catalysis such as CO oxidation. In the third part, in situ studies under batch reaction conditions are discussed, which are complemented by *operando* studies under flow conditions (fourth part).

3.2 Surface-Sensitive X-ray Diffraction as in situ Tool

Surface-sensitive X-ray diffraction techniques can be divided in four different submethods, which allow to probe different properties of the surface. Surface X-ray diffraction (SXRD) provides crystallographic information on the atomic structure and composition of surfaces, interfaces, and nanoparticles [1, 3–5]. SXRD is complemented by X-ray reflectivity sensitive to the total electron-density profile perpendicular to the surface, containing information on roughness, layer thickness, nanoparticle average height, and surface coverage [6, 7]. In grazing incidence X-ray diffraction the information depth probed can be changed from nm to μm by a variation of the incident and the exit angle with respect to the surface [2, 8]. In addition, the signal-to-noise ratio in diffraction experiments can be optimized by a grazing incidence diffraction geometry. Finally, in grazing incidence small angle X-ray scattering (GISAXS) experiments the lateral surface morphology is probed [9].

Surface X-ray diffraction, grazing incidence X-ray diffraction, and grazing incidence small angle scattering experiments are traditionally performed using synchrotron radiation because of the required high brilliance of the X-ray beam to detect the diffraction signal from single atomic layers or very small nanostructures. Practically all third-generation synchrotron radiation sources possess end stations, which permit to perform SXRD, GIXRD and GISAXS experiments in combination with customized user sample environments [10]. X-ray reflectivity measurements are routinely performed using X-ray lab sources and with the advent of higher-brilliance micro-focus X-ray tubes also SXRD, GIXRD, and GISAXS experiments become feasible in the lab, at least for high-Z materials.

3.2.1 Basics of Surface X-ray Diffraction

The principles of surface X-ray diffraction (SXRD) are based on the fact that X-ray diffraction from a half-infinite crystal terminated by a surface (see Fig. 3.1a), is intrinsically sensitive to the atomistic structure of the surface. A real-space lattice made up by lattice vectors $\boldsymbol{a}$, $\boldsymbol{b}$, $\boldsymbol{c}$ is connected to the corresponding reciprocal space vectors $\boldsymbol{a}^*$, $\boldsymbol{b}^*$, $\boldsymbol{c}^*$ by the Laue equations [11]. A 3D infinite crystal gives (in kinematical approximation) rise to δ function-like Bragg reflections (blue circles in the reciprocal lattice in Fig. 3.1b). For a semi-infinite crystal, the Bragg reflections are not represented by δ functions any more and the so-called crystal truncation rods (CTRs) arise because of the truncation of the crystal by the surface. They run perpendicular to the crystal surface (HKL) plane through the Bragg reflections, as indicated by the green lines in Fig. 3.1b. In case the overlayer exhibits a different periodicity, additional surface rods arise (red dashed lines in Fig. 3.1b), which are sensitive to the structure of the overlayer only. In case of a commensurate structure the CTRs carry in addition information on the registry of the overlayer with respect to the substrate and the interfacial structure.

In a scattering experiment the scattering vector $\boldsymbol{q}$ is defined as $\boldsymbol{q} = \boldsymbol{k}_f - \boldsymbol{k}_i$, where the incident and exit wave vectors of the elastically scattered X-rays are given by $\boldsymbol{k}_{i,f}$, respectively ($|\boldsymbol{k}_{i,f}| = \frac{2\pi}{\lambda}$ with X-ray wavelength λ). To probe the reciprocal lattice, the Bragg condition $\boldsymbol{q} = \boldsymbol{G}$ has to be fulfilled, where $\boldsymbol{G}$ is a reciprocal lattice vector. The experiment can in principle be realized by any type of diffractometer possessing three independent degrees of freedom for the sample and detector stages. For practical reasons, most of the surface diffraction experiments are carried out on six-circle diffractometers in z-axis mode [1, 12]. Two out of the six circles are needed to orient the surface normal of the sample along the rotation axis θ, see Fig. 3.1c. The third axis, kept fixed during the experiments, is the incident angle μ. Typically, small incident angles are chosen, to reduce background scattering from the bulk and to increase the signal-to-background ratio. Note, that the surface sensitivity of the technique does not depend on the actual value of the incident angle—the reciprocal lattice of a two dimensional or half-infinite system is intrinsically surface sensitive.

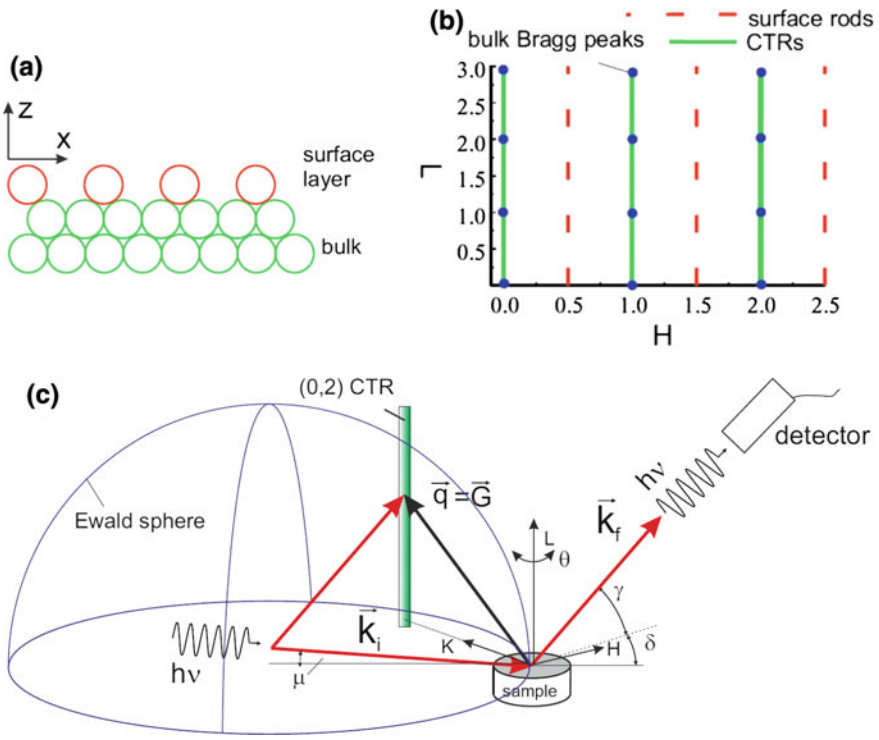

Fig. 3.1 **a** Truncated crystal with reconstructed adlayer. **b** Reciprocal lattice of the real space structure in (**a**). **c** *Z*-axis surface X-ray diffraction geometry

The intersection of the CTR with the Ewald sphere defines the direction of the diffracted X-rays (wave vector $\boldsymbol{k}_f$), which are collected by the detector rotating in δ and γ. For crystallographic structure-factor measurements, the diffractometer is moved to a specific (H, K, L) position and a θ scan is performed. The amplitude of the structure factor is obtained after integration of the θ scans and applying standard correction factors [5]. Alternatively, the structure factor can be collected using a two-dimensional detector [13, 14].

The diffracted CTR intensity can be calculated in a straightforward way [3]:

$$I(\boldsymbol{q}) \propto |F(\boldsymbol{q})|^2 \cdot \frac{1}{sin^2(\pi L)} \cdot \delta(\boldsymbol{Q}_{\parallel} - \boldsymbol{G}_{\parallel}) \tag{3.1}$$

$F(\boldsymbol{q})$ represents the structure factor of the unit cell, the second term is the CTR term, depending on the continuous reciprocal-lattice coordinate L in units of c^*. It diverges at the positions of the bulk Bragg reflections at integer values of L. The third term is a δ function for the momentum transfer $\boldsymbol{Q}_{\parallel}$ parallel to the surface, because in the surface plane the Bragg condition $\boldsymbol{Q}_{\parallel} = \boldsymbol{G}_{\parallel}$ has to be fulfilled to observe scattered

intensity ($\boldsymbol{G}_{\parallel}$ represents the component of the reciprocal lattice vector in the surface plane).

The following information can be obtained from a surface X-ray diffraction experiment by a trial-and-error fit to the data or by the use of so-called 'direct methods', based on phase-retrieval algorithms [15]: atomic positions, surface structure with pm resolution, surface composition, surface and interface roughness, thermal vibration amplitudes, and the overlayer registry to the substrate. In general, all additional experimental and theoretical information available is used as an input for the fit, because in surface crystallography only a smaller number of structure factors can be obtained from the experiment, as compared to a bulk crystal structure analysis for a comparable number of atoms in the unit cell.

3.2.2 X-ray Reflectivity and Grazing Incidence Diffraction

A: X-ray Reflectivity

X-ray reflectivity is a standard technique to characterize layered structures with sub-nm resolution. In specular reflectivity experiments, the reflected intensity is recorded as a function of the incident angle μ with respect to the surface in symmetric condition ($\mu = \gamma$, $\delta = 0$, see Fig. 3.1c). For small angles (below 1° for most materials at a photon energy of 10 keV) total external reflection occurs and the Fresnel equations can be applied to calculate the reflected intensity [16–18]. In off-specular reflectivity experiments ($\mu \neq \gamma$, $\delta = 0$) an additional momentum transfer component is applied parallel to the surface along the incident beam direction. The combination of both techniques gives morphological information (independent of the crystallinity of the sample) with 0.1 nm resolution on: layer thickness, total-layer electron density, interfacial mean square roughness perpendicular to the surface, and lateral interfacial correlations [19] (height-height correlation function).

B: Grazing Incidence X-ray Diffraction

For small μ and/or γ (in the order of the critical angle α_c for total external reflection) and finite in-plane momentum transfer $\boldsymbol{Q}_{\parallel}$ (see Fig. 3.1b) the incident and the exit beam undergo strong refraction effects and the diffracted intensity can no longer be treated in kinematical approximation. The distorted-wave Born approximation has to be used instead, which includes refraction effects of the incident and the exit beam fully dynamically and the diffraction process itself in kinematic approximation. The following general expression can be derived for the scattered intensity [2]:

$$I(\boldsymbol{Q}') \sim |T(\mu)|^2 \cdot |T(\gamma)|^2 \cdot S(\boldsymbol{Q}') \,. \tag{3.2}$$

Here $|T(\mu, \gamma)|$ denotes the optical transmission function of the incident and exit beam, respectively [20]. Note that (3.2) is symmetric in μ and γ because of the reciprocity of the X-ray light path. $S(\boldsymbol{Q}')$ denotes the kinematical structure factor which depends on the momentum transfer $\boldsymbol{Q}'$ inside the material. $S(\boldsymbol{Q}')$ can describe any diffraction process, like Bragg scattering from near-surface lattice planes, small angle

scattering, or interstitial diffuse scattering. Most important for grazing-incidence diffraction, the diffraction signal $S(\boldsymbol{Q}')$ can be obtained with a depth resolution from nm to μm, depending on the choice of the incident and the exit angles μ and γ [2]. Over the scattering depth, the component of the electrical wave field perpendicular to the surface is exponentially damped. For SXRD and SAXS the grazing-incidence geometry results in an improved signal-to-noise ratio.

C: Grazing Incidence Small Angle Scattering

For grazing incidence small angle X-ray scattering (GISAXS), an additional (small) momentum transfer $\boldsymbol{Q}_{\|}$ ($\delta \neq 0$) is present. For GISAXS, $\boldsymbol{Q}_{\|}$ is much smaller than typical reciprocal-lattice vectors from atomic planes. From GISAXS experiments combined information on nanoparticle size and distance distributions can be obtained [9]. In general, a quantitative analysis of GISAXS data is possible, but it is hampered by the sometimes difficult deconvolution of the distance and the size information of the nanostructures.

3.2.3 *In situ and* Operando *Sample Environments*

In this section the design of different in situ X-ray diffraction chambers is discussed, which allow on the one hand preparation of surfaces and nanostructures under controlled ultrahigh vacuum (UHV) conditions, and which are on the other hand compatible with atmospheric pressures thus bridging the pressure gap of 12 orders of magnitude from 10^{-9} mbar to 1 bar [21]. Two concepts are followed: For the first the chamber is operated at pressures above 10^{-3} mbar as batch reactor [22]. The second type of chamber can be run as a true flow reactor from about 10^{-2} mbar (when working with diluted gases) up to 1 bar [23].

Figure 3.2a shows a photograph of experimental equipment, available at beamline ID03 at the ESRF, that enables studies of model catalysts under higher pressures of a gas or semi-realistic reaction conditions in a batch reactor using SXRD [22]. The batch reactor consists of a 360° 2-mm-thick beryllium window with a geometry that allows operation of the chamber under external pressure of the atmosphere when the chamber is in vacuum and under internal pressure when the chamber is pressurized. The beryllium window is almost transparent to hard X-rays due to its low atomic number. The sample surfaces can be prepared in UHV with traditional surface-science recipes such as ion sputtering, annealing, etc. The batch reactor can be operated in a pressure range between 10^{-9} mbar and 5 bar to study surface structures of the adsorbed gases and possible modifications of the substrates induced by the surrounding gas. The sample can be heated by a ceramic heating plate and can reach a temperature of 1000 °C under vacuum and ~550 °C under 1 bar of pressure. The gas composition within the pressurized part of the chamber can be analyzed by a mass spectrometer simultaneously as the sample surface is probed by the X-rays. The chamber itself and its technical accessories are mounted onto a diffractometer to perform diffraction experiments with large scattering angles, allowing for exploring large regions of reciprocal space. Figure 3.2b shows the batch chamber in its high pressure oxidation variant. The sample sits inside a free standing, X-ray transpar-

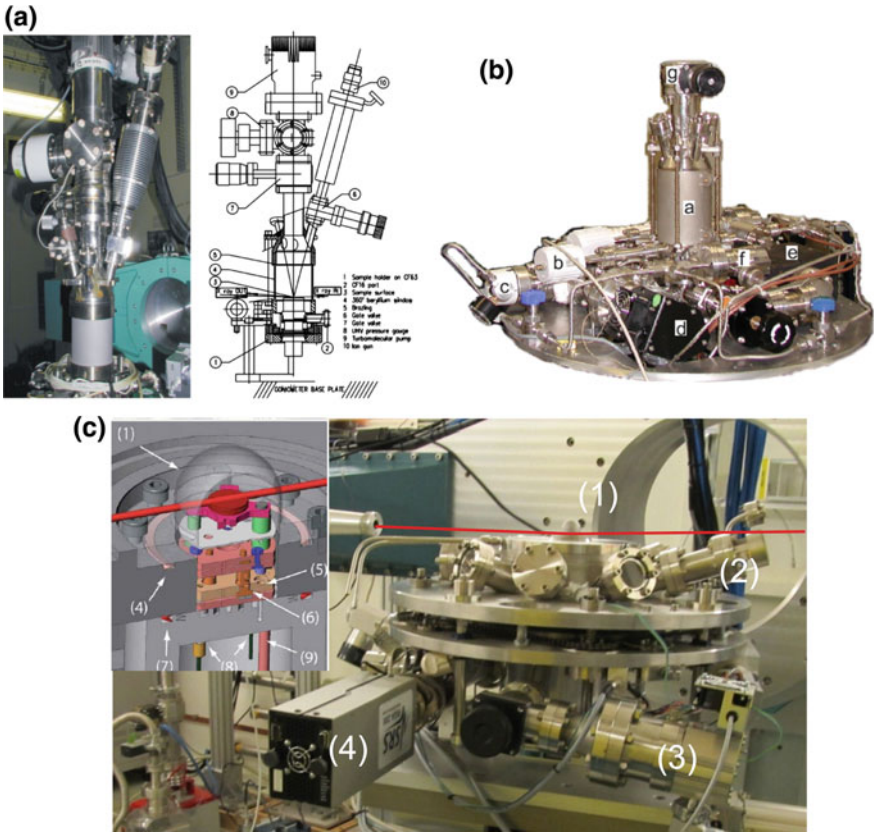

Fig. 3.2 **a** UHV-to-atmospheric-pressure X-ray diffraction chamber for batch catalysis experiments (adopted from [22]) **b** modified version of batch chamber for pure oxidation experiments **c** UHV-to-atmospheric-pressure flow reaction chamber mounted on the heavy diffractometer at P09, PETRA III (DESY). *Inset* schematic zoom of the reaction volume

ent 2-mm-thick Beryllium cylinder (a). The pressure is monitored from UHV up to 10^{-3} mbar by a cold cathode gauge (c) and up to 1 bar by two independent capacitive pressure gauges (b). The chamber is pumped via a turbo molecular pump (d) which can be isolated from the chamber by an angular valve. For controlled sample transfer from a preparation chamber to the synchrotron beamline the chamber can be pumped by an ion getter pump (e). Gases can be dosed through rough- and fine-adjustable leak valves. On top of the chamber, an ion sputter gun for surface cleaning or an evaporator can be mounted. The Al_2O_3-encapsulated Pt-wire heater allows sample temperatures up to ~900 K. The samples are mounted onto inconel sample holders and they can be brought into direct contact with a thermocouple for temperature control. A larger batch reactor (volume 5.5 l) for surface X-ray diffraction is discussed in [24].

For pure oxidation studies the batch chamber is a nice possibility to bridge the pressure gap, as well as for relatively slow catalytic reactions. Technologically relevant processes, however, take place under flow conditions with controlled gas mixtures. Therefore a UHV-compatible flow reaction chamber was developed at beamline ID03, ESRF, as pictured in Fig. 3.2c [23]. The chamber can be operated in two different configurations: In the first, the top flange (1) is moved up to a position, where the surrounding flanges carrying the sputter gun (2) and other auxiliary equipment look at the sample position. In this configuration the sample surface can be prepared in a routine way known from UHV surface-science studies. Also in this setup, the sample can be heated up to 1200 K by a PBN-C heater with direct sample mounting to the heater plate. A thermocouple can be attached directly to the sample. The chamber is pumped by a turbo molecular pump (3) and a residual gas analyzer (4) is attached to the system.

In the second configuration the top flange is moved down, thereby sealing off the top part of the chamber with the Be dome (5) from the UHV part below by a gasket-carrying piston inside the chamber. Two capillaries are connected to the top part of the chamber, allowing to flow controlled gas mixtures, while performing X-ray diffraction experiments. For the gas flow a computer controlled gas system is used, which allows gas mixtures of several gases with individual flow control (up to a total integrated flow of 200 ml/min), as well as total pressure control inside the reaction volume from 1 mbar to 1.3 bar. The gas composition inside the reaction volume can be detected by the mass spectrometer inside the UHV part of the chamber by controlled leaking in from the reaction volume. Similar setups now exist at the Nanolab at DESY, at the division of Synchrotron Radiation Research at Lund University and beamline SIXS at SOLEIL.

3.3 In situ Near-Atmospheric-Pressure Oxidation of Transition Metal Surfaces and Nanoparticles

In catalytic oxidation reactions of 3d, 4d, and 5d catalyst materials such as Cu, Ag, Pd, Rh, Ru, Pt, or Ir, it is frequently debated whether the oxide of the metal is the most active phase [25, 26]. These noble metals are difficult to oxidize at low, near UHV oxygen pressures, which explains why their interaction with oxygen has not been well studied in the past by traditional surface science techniques. As a prerequisite for reaction studies it is therefore important to investigate the oxidation behavior of noble metals at (near-)atmospheric pressures. Recent results discussed here focused on model systems such as low-index single-crystal surfaces. Increasing complexity was introduced by the investigation of vicinal surfaces and epitaxial nanoparticles with well-defined shape on single crystal oxide supports.

3.3.1 Transition-Metal Low-Index Surfaces

3.3.1.1 Oxidation of Low Index Ag

Silver is an important catalyst for several reactions, like ethylene epoxidation and the partial oxidation of methanol to formaldehyde [27]. Both reactions take place at atmospheric oxygen pressures and at temperatures from 500 to 900 K. The active oxygen species has been a matter of debate in the literature for a long time and it is still unclear up to date [28]. The interaction of oxygen with Ag(111) was studied by low-energy electron diffraction (LEED) already in the early seventies and a p(4x4) LEED pattern was observed [29–33]. Based on previous LEED, X-ray photoelecrton spectroscopy (XPS), and scanning tunneling microscopy (STM) investigations in combination with density functional theory (DFT) calculations the p(4x4) reconstruction was interpreted as an epitaxial $Ag_2O(111)$ layer, rotated by 30° with respect to the hexagonal unit cell of the Ag(111) substrate. The SXRD measurements together with new STM data disproved the $Ag_2O(111)$ layer model and gave evidence for a different structural model based on nanometric Ag(111) triangles, occupying faulted and unfaulted sites of the fcc stacking sequence [34, 35]. Oxygen ions occupy the furrows in between the Ag triangles in line with a chemisorption-induced reconstruction. The model is also supported by DFT calculations taking van der Waals interactions between Ag atoms into account. Furtheron the formation of epitaxial bulk oxide $Ag_2O(111)$ was observed after exposing the Ag(111) surface to atmospheric oxygen pressures at 800 K and cooling to room temperature [36]. The bulk oxide grows in coexistence with an ultrathin surface oxide layer, which very likely exhibits a trilayer surface oxide structure.

The (100) surface was exposed to near-atmospheric oxygen pressures at 440 K and it was studied by in situ SXRD [37]. A disordered form of a $p(2\sqrt{2} \times \sqrt{2})$ missing row reconstruction could be observed in the in situ SXRD experiment at 10 mbar O_2 pressure and 440 K. The surface undergoes a reversible transformation to the missing-row-like structure by increasing and decreasing the oxygen pressure. Under conditions, at which the missing row structure is observed, no evidence for the formation of subsurface, interstitial oxygen was detected. An ordered $p(2\sqrt{2} \times \sqrt{2})$ missing-row reconstruction was reported previously from low temperature LEED and X-ray photoelectron diffraction experiments [38]. Similar oxygen-induced order - disorder transitions were observed for the Cu(100) surface, as followed by SXRD [39].

3.3.1.2 Low-Index Pd Surfaces

Pd exhibits a high reactivity for CO oxidation, which is one of the basic catalytic reactions. As a prerequisite to CO oxidation under realistic reaction conditions, the interaction of oxygen with Pd surfaces up to atmospheric pressures needs to be understood. For Pd(100) and Pd(111) the formation of O-Pd-O trilayers is reported in the

literature [40, 41]. Both have in common, that twofold and fourfold coordinated Pd atoms coexist (note, that in bulk PdO the Pd atoms are fourfold coordinated). On Pd(100) a surface oxide in a $(\sqrt{5} \times \sqrt{5})$ arrangement is formed, which exhibits a structure close to the (101) plane of PdO bulk oxide. One of the key questions of today's research in catalysis is whether chemisorbed oxygen or such surface oxide layers play a role for catalytic processes or nanometric layers of bulk oxide PdO instead [42–44]. Therefore, the stability of the surface oxide layers was studied as a function of the oxygen chemical potential μ [45–48]. Figure 3.3a shows the transition of the surface oxide to the bulk oxide for Pd(111) as a function of the oxygen pressure at 673 K. The surface oxide forms a $\sqrt{6} \times \sqrt{6}$-like overlayer with Pd_5O_4 stoichiometry on Pd(111) [40], which gives rise to a distinct surface X-ray diffraction signal. The signal from the epitaxial PdO bulk oxide can be discriminated as well. The results from such pressure- and temperature-dependent measurements are summarized in the stability diagram in Fig. 3.3b. The transition from the surface covered with chemisorbed oxygen to the surface oxide can be described by a line of constant oxygen chemical potential [48] of –1.24 eV, indicating local equilibrium. On the contrary, the bulk oxide formation is kinetically hindered over a wide temperature range and it does not take place below 500 K because the surface oxide is

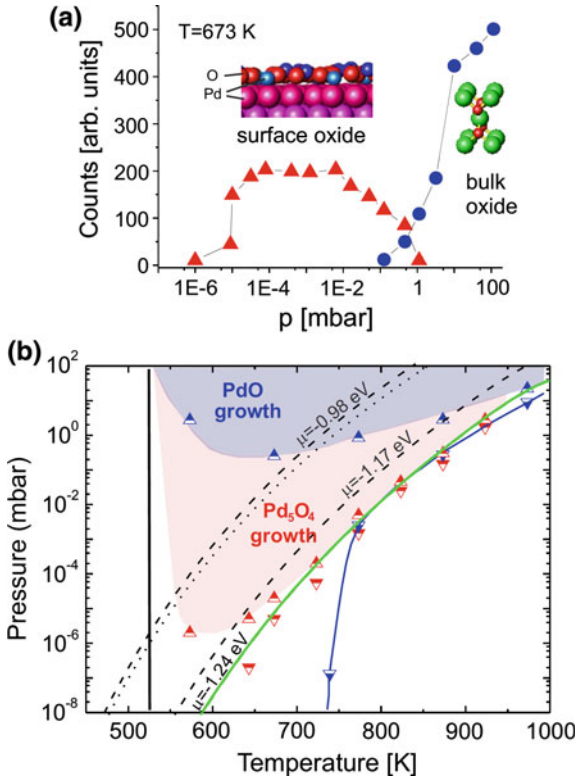

Fig. 3.3 **a** Experimental observation of the surface oxide to bulk oxide transition at constant temperature as a function of the oxygen pressure (*triangles*: surface oxide signal, *circles*: bulk oxide signal), **b** experimental stability diagram derived from pressure dependent measurements at different temperatures (*upward triangles*: oxygen pressure increasing, *downward pointing triangles*: oxygen pressure decreasing). From [48]

passivating the surface. At 973 K kinetic barriers are lifted and the bulk oxide forms directly without the intermediate surface oxide. Similar in situ SXRD experiments were performed on the Pd(110) surface, pointing towards a reduction of the kinetic barriers for bulk oxide formation, as compared to Pd(100) and Pd(111) [49].

3.3.1.3 Oxidation of Low Index Rh Surfaces

Rh oxides involved in catalytic oxidation reactions typically form at oxygen pressures of 10^{-3} mbar and above at application-relevant temperatures. The Rh(100) surface undergoes a transformation from a p(2×2) to a p(3×1) reconstruction with increasing oxygen exposure. Close to the chemical potential for bulk oxide formation, a c(2×8) reconstruction is observed [50]. A detailed atomistic model of this structure was determined by a combination of DFT calculations, surface X-ray diffraction, LEED, high-resolution core-level spectroscopy (HRCLS), and STM [51]. The structural model is based on a hexagonal oxygen-Rh-oxygen trilayer, similar to the trilayers formed on Pd(100) and Pd(111). The hexagonal layer is slightly distorted to accommodate a c(2×8) structure and it forms in two domains rotated by 90°. Figure 3.4a shows the the structural model of the trilayer surface oxide which

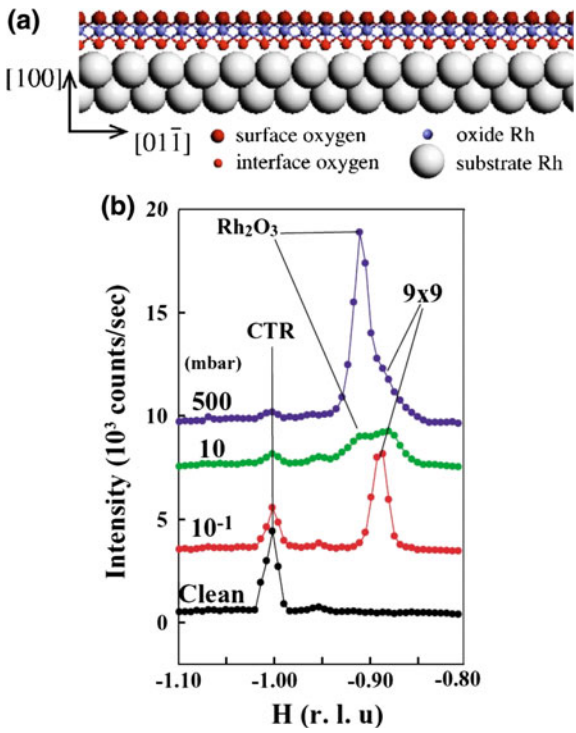

Fig. 3.4 **a** Structural model for the surface oxide layer on the Rh (100) surface, **b** SXRD data showing the transition from the Rh surface oxide to Rh_2O_3 bulk oxide on Rh(111). Adopted from [45]

is also observed on Rh(110) and Rh(111), pointing towards the high stability of this structure [45, 52]. The transition of the surface oxide on Rh(111) to Rh_2O_3 bulk oxide as a function of the oxygen pressure at 800 K is illustrated in Fig. 3.4b: In scans with momentum transfer in the surface plane the surface oxide signal gives rise to a reflection at H = 0.89 reciprocal lattice units at 10^{-1} mbar, which shifts to H = 0.91 for the Rh_2O_3 bulk oxide at 10 mbar O_2 pressure [45].

3.3.1.4 Oxidation of Pt(111) and Ir(111)

Pt and Ir are important 5d transition-metal catalysts for CO oxidation [53, 54]. In addition, Pt coatings are discussed as protective layers in aggressive chemical environments, for example to protect the electrodes of sparkling plugs in cars and to increase their lifetime. The oxidation of a Pt(111) single crystal and epitaxial, (111)-oriented Pt films on α-Al_2O_3 were studied by in situ surface X-ray diffraction at near-atmospheric pressures [55]. The oxidation of the Pt(111) surface is kinetically strongly hindered and an ultrathin α-PtO_2 layer forms at 910 K at 0.5 bar O_2 pressure. A structural analysis reveals that the oxide consists of one α-PtO_2 unit cell, which is compressed in the direction perpendicular to the surface and distorted in the surface plane.

A detailed SXRD study of the oxidation of the Ir(111) surface gave evidence of the formation of an O-Ir-O trilayer also for this system at 575 K in an intermediate oxygen pressure regime up to 1 mbar O_2 pressure [56]. At higher temperatures the formation of epitaxial bulk IrO_2 islands in different orientations with thicknesses in the range of 5–10 nm was observed.

3.3.2 Oxidation of Vicinal 4d Transition-Metal Surfaces

Vicinal surfaces provide a very elegant way to mimic defects such as steps and corners between different nanoparticle facets, since the geometry of the defect can be chosen over a wide range by the vicinal angle and orientation.

3.3.2.1 Pd and Rh Vicinal Surfaces

The oxidation of Pd(553) and Pd(112) vicinal surfaces was studied employing the powerful combination of in situ surface X-ray diffraction, high resolution scanning tunneling microscopy, and core level spectroscopy, together with DFT calculations [57, 58]. The fcc(553) surface exhibits threefold coordination on terrace and step sites whereas the (112) surface shows (100) type steps with fourfold symmetry. Both the (553) and (112) Pd surfaces are found to be stable after preparation under UHV conditions. At 600–700 K and 10^{-6} mbar oxygen pressure the (553) surface transforms into (332) facets, which are decorated by a surface oxide layer, exhibiting a

12 times larger unit cell along the terraces as compared to the substrate resembling the $\sqrt{5}$ trilayer forming on the Pd(100) surface. At pressures of 1 mbar epitaxial and polycrystalline bulk oxide formation sets in. The epitaxial oxide islands are tilted with respect to the substrate and grow in PdO(012) orientation. The morphology of the Pd(112) surface is also strongly influenced by the oxidation conditions: At 673 K, upon exposure to oxygen at pressures from 2×10^{-8} to 5×10^{-5} mbar, the (112) surface undergoes a massive rearrangement and (113)- and (335)-type facets are formed. Further increase of the O_2 partial pressure leads to a new rearrangement into (111)- and (113)-type facets. Bulk oxide formation is observed at 5 mbar O_2 pressure and T = 523 K, which is below the bulk oxide formation temperature of low-index (100) and (111) surfaces. This elucidates the role of steps towards lifting of kinetic barriers for bulk oxide formation.

For comparison, the oxidation of the Rh(553) surface was investigated by SXRD from UHV to near-atmospheric pressures [59]. At 380 °C and 10^{-6} mbar O_2 pressure the formation of (331) facets is observed along with an oxygen-induced restructuring along the steps. At higher pressures above 10^{-3} mbar and a temperature of 500 °C the formation of the O-Rh-O trilayer surface oxide stabilizes larger (111) facets, in line with the particular stability of this interface.

3.3.3 Nanoparticle Oxidation Across the Pressure Gap: Pd, Rh and Pt Nanoparticles on MgO(100) and $MgAl_2O_4$(100)

State of the art in situ structural studies of catalytic reactions are performed on powder samples made up by sub-micron grains of supporting oxide particles covered with nanometer-sized metal/alloy particles [60]. To obtain a deeper insight into the basic processes occurring during chemical reactions on nanoparticles, one possible approach is to replace the real catalyst by epitaxial nanoparticles with a well-defined orientation relationship and size distribution, grown by physical vapor deposition onto single crystal oxide supports [61]. Such a system allows *operando* X-ray studies under realistic pressures at elevated temperatures, giving detailed insight into structural and morphological changes during the reaction. Fcc metals like Pd, Rh and Pt grow on MgO(100) and $MgAl_2O_4$(100) in the (100) direction with truncated octahedral shape exposing mainly (111)- and (100)-type facets under UHV conditions.

Using reciprocal space mapping, Pd nanoparticles on MgO(100) with diameters in the range of 5–9 nm were shown to form nanometer sized (112)-type facets under 10^{-5} mbar oxygen exposure and 570 K, which is reversible under CO exposure [62]. In contrast, for Rh nanoparticles (100)- and (111)-type facets are stabilized under similar conditions by the formation of a surface oxide trilayer O-Rh-O shell, which was detected in corresponding X-ray diffraction line scans [63]. The Rh surface oxide formation is accompanied by a nanoparticle shape change increasing the (100) sur-

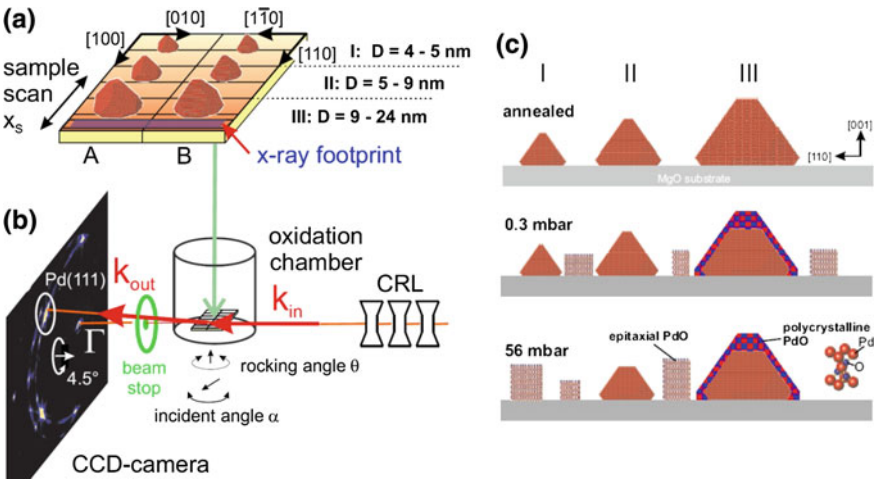

Fig. 3.5 Oxidation of Pd nanoparticles [65]. **a** Combinatorial sample architecture with nanoparticle stripes of different average diameter. **b** High energy X-ray diffraction scheme using a 2D detector. **c** Oxidation scenario for different nanoparticle size regimes

face area, which can be rationalized on the basis of the higher stability of the surface oxide on the Rh(100) surface [64]. Also in this case, the shape change is found to be reversible under CO exposure.

For the systematic investigation of size- and composition-dependent phenomena, a novel approach was developed combining high-energy grazing incidence X-ray diffraction with a combinatorial sample architecture. The size-dependent oxidation of epitaxial Pd nanoparticles on MgO(100) was investigated in the regime from 4–24 nm, revealing that the formation of a polycrystalline passivation layer is only observed for particle sizes above 9 nm [65]. For smaller particles the growth of epitaxial PdO is found instead (Fig. 3.5).

Alloying of Rh with Pd leads to a very different oxidation behavior: The composition-dependent oxidation of Pd-Rh nanoparticles on $MgAl_2O_4(100)$ in the size regime 5–10 nm gave evidence for a preferential Rh oxide formation accompanied by oxidation-induced Rh surface segregation [66]. Pd oxide formation was only observed for pure Pd nanoparticles. For epitaxial Pt nanoparticles on MgO(100) the formation of higher-index facets was observed after oxidation at 570 K in the pressure regime of 10^{-3} mbar to 0.5 bar, which was found to be non-reversible under CO exposure in contrast to the Pd and Rh case [67]. The formation of epitaxial PtO_2 and Pt_3O_4 was observed, which was stable under vacuum annealing up to 923 K, pointing to strong kinetic barriers for their reduction.

3.4 In situ Catalytic Studies Using Batch Reactors

In this chapter examples of in situ catalytic reactions using a batch reactor by combining SXRD and mass spectrometry will be described. Here we will focus on Pt, Ru, Pd, and Rh surfaces during CO oxidation reactions as well as the Ru surface during HCl oxidation. As pioneering work it was demonstrated that the CO induced (2x1) reconstruction on Ni(110) is at room temperature stable up to atmospheric pressures [68]. The hydrogenation of butadiene over a $Ni_{0.92}Pd_{0.08}(110)$ model catalyst was investigated in batch mode [69], but this is not discussed in detail here. At the end of the section, results on batch experiments of model nanoparticle catalysts on single crystal oxide supports are presented.

3.4.1 CO Oxidation Over Pt

The first in situ SXRD CO-oxidation experiment using a batch reactor and a single crystal surface as a model catalyst was presented in 2005 [70]. In this study, a Pt(110) surface during CO oxidation at pressures up to 0.5 bar and temperatures up to 350 °C was studied. Prior to the CO oxidation experiments, the initial oxidation of the surface was investigated. At an oxygen pressure of 500 mbar and a sample

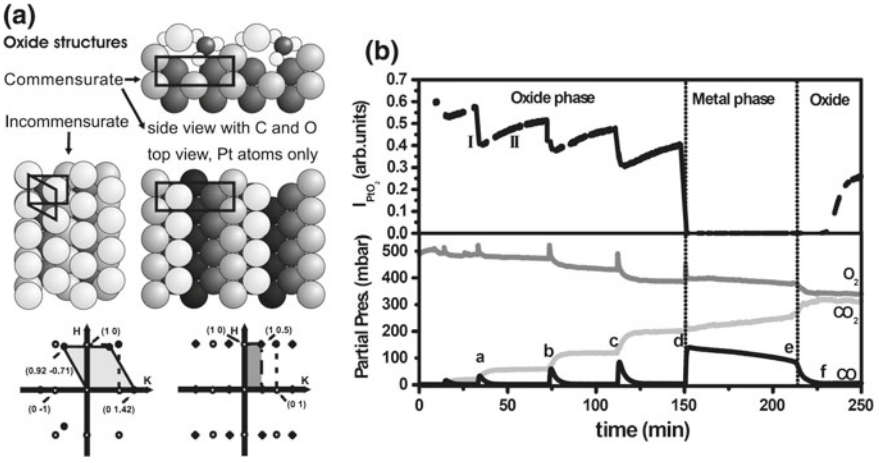

Fig. 3.6 **a** *Bottom left* In-plane reciprocal space map of the Pt(110) substrate (*open circles*), with the incommensurate, quasihexagonal oxide overlayer (only Pt atoms are shown, *solid circles*). *Bottom right* The in-plane reciprocal space map of the (1×2), commensurate oxide overlayer (*crosses*). The ball models show the real-space structures of the two oxides. **b** Simultaneously measured X-ray diffraction intensity at (0, 1.42, 0.5) from the quasihexagonal oxide (*top panel*) and partial pressures of CO, O_2, and CO_2 (*bottom panel*). Separate CO pulses were admitted to the reactor, which was initially filled with 500 mbar of O_2 at a temperature of 350 °C. The sharp peaks in P_{O2} are an artefact due to the sudden increase of total pressure at each CO pulse. From [70]

temperature of 350 °C, the formation of an incommensurate quasihexagonal α-PtO_2 oxide layer was observed. The structure found is described in Fig. 3.6. When CO was introduced together with oxygen, the catalytic oxidation of the CO into CO_2 could be observed. The experiment is shown in Fig. 3.6b, in which the intensity of the oxide peak (top part) is probed simultaneously with the O, CO and CO_2 pressures as a function of time. When the oxidized Pt surface is exposed to relatively moderate amounts of CO (Fig. 3.6b, "a" to "c"), the oxide layer is roughened by the reaction, but the surface remains oxidized and exhibits a high reaction rate. When exposed to higher pressures of CO (Fig. 3.6b "d"), the oxide is completely reduced, as indicated by the section termed metallic phase in Fig. 3.6b. A simultaneous decrease in the reactivity was observed. After point "d", the CO is consumed in the batch reactor by the oxidation into CO_2, and the CO/O pressure ratio is continuously reduced, since two CO molecules are consumed by one O_2 molecule. When the CO pressure is sufficiently low, the surface re-oxidizes, which can be seen by the re-appearance of the diffraction signal from the incommensurate α-PtO_2. However, the reaction rate calculated from the increase in the CO_2 signal increases sharply about 20 min before the re-appearance of the oxide signal. Instead, a set of new diffraction peaks could be detected simultaneously with the increase in reaction rate (not shown). These peaks were found to correspond to a commensurate (1×2) surface structure. The structure could only be observed under reaction conditions, any attempt to quench the structure by cooling and evacuating the chamber resulted in the disappearance of the diffraction spots. By structural measurements during the reaction combined with DFT calculations, the commensurate structure shown in Fig. 3.6a (right) could be proposed, which involves the presence of one carbonate ion per unit cell. These observations show that in situ measurements under actual reaction conditions are crucial for a meaningful investigation of the surface structure and chemical behavior of this model catalyst. Clearly, the presence and role of the commensurate (1×2)-layer could not have been found either in experiments under UHV or in so-called pre- and post-reaction experiments.

3.4.2 Ru

3.4.2.1 CO Oxidation Over Ru

The oxidation and reduction of a Ru(0001) surface was investigated by He et al. [71] paving the way for CO oxidation experiments over the Ru(0001) surface at realistic conditions using SXRD. The catalytic CO oxidation over the Ru(0001) surface was investigated in detail using the above batch reactor [72, 73]. In essence, the studies were conducted to compare the CO_2 production in the presence of the so-called metallic phase and in the presence of an oxidized Ru(0001) surface, the RuO_2(110) surface.

In a first set of experiments the investigations were made under isothermal conditions [71]. An example of the experiments is shown in Fig. 3.7. The temperature was

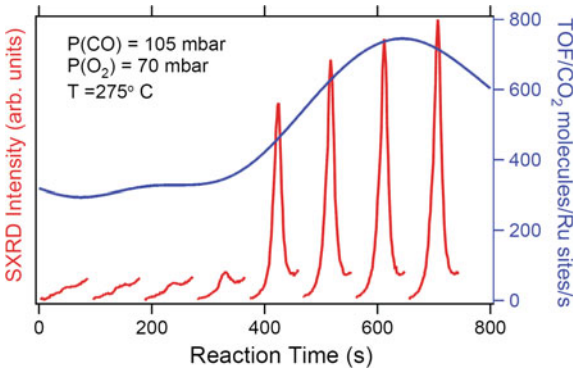

Fig. 3.7 The activity of CO oxidation and the surface structure of the Ru(0001) surface during isothermal conditions. The experiment starts with $P(O_2) = 70$ mbar and $P(CO) = 105$ mbar at a sample temperature of 275 °C. From the CO_2 partial pressure and a gas temperature of 25 °C the TOF can be determined. The $RuO_2(110)$ can be identified after about 200 s in the repetitive l-scans at h = 0.73. The appearance of the $RuO_2(110)$ reflection can be correlated to an increase in the TOF. From [74]

kept constant at 275 °C with initial O_2 and CO partial gas pressures of 70 and 105 mbar, respectively. At the beginning of the experiment, the activity is low, but not zero. Since twice as many CO molecules are consumed compared to O_2, the environment becomes increasingly oxidizing, and after 200 s the surface transforms from the metallic state into the $RuO_2(110)$ state, in conjunction with a significant increase of the CO_2 production and turnover frequency (TOF). This observation indicates that the presence of a $RuO_2(110)$ phase results in a more active phase than the non-oxidized surface.

Similar experiments were done at different temperatures, and it was found that the metallic and the $RuO_2(110)$ phase had an approximately equal TOF at 255 °C but that the $RuO_2(110)$ phase had a higher TOF at 275 °C and higher temperatures. Furthermore, a significant reaction-induced temperature increase of the sample was observed at temperatures of 275 °C and higher. In a second set of experiments [72] the effect of changing the temperature of the sample was investigated. Also in this study it was concluded that the metallic and the $RuO_2(110)$ phases were almost equal at temperatures below 245 °C while at higher temperatures the $RuO_2(110)$ was more active.

3.4.2.2 HCl Oxidation Over Ru

The oxidation of hydrochloric acid (HCl) by oxygen (O_2) into water (H_2O) and chlorine (Cl_2), the so-called Deacon process [75], is an important reaction for the industrial chlorine production. Recently, it was observed that RuO_2-covered TiO_2 leads to an efficient catalyst for the Deacon process [76]. Fundamental studies of the HCl

interaction with the $RuO_2(110)$ surface have shown that Cl atoms replace the bridging oxygens in the top-most $RuO_2(110)$ layer [77], and that the oxidation of HCl into H_2O and Cl_2 appears to follow the Langmuir-Hinshelwood (LH) mechanism along the rows of under-coordinated Ru sites [74, 78], at least under UHV conditions. The stability of the $RuO_2(110)$ during HCl oxidation at more realistic conditions was studied [79] using in situ SXRD in a similar batch reactor as described above, the difference being a replacement of the cylindrical X-ray Be window with a 1 mm thick Al window, to avoid to brittle the Be due to high HCl exposures. It could be shown that in pure HCl at a pressure of 1 mbar both the $RuO_2(110)$ and the $RuO_2(100)$ are stable up to a temperature of 325 °C, but are reduced at temperatures above 325 °C. By introducing oxygen, the thickness of the $RuO_2(110)$ and $RuO_2(100)$ films were even observed to increase at temperatures as high as 345 °C at oxidizing reaction conditions. By combining the SXRD data with online mass spectrometry the mean turnover frequencies could be determined in the presence of the $RuO_2(110)$ and $RuO_2(100)$ surfaces, indicating that the HCl-oxidation is structure insensitive.

3.4.3 CO Oxidation Over Rh

The CO oxidation over Rh catalysts has been studied for a long time under UHV [80, 81] as well as under more realistic conditions [82]. However, very little is reported on the surface structures of Rh model catalyst surfaces under more realistic pressure conditions.

The surface structure over Rh(111) and Rh(100) surfaces during CO oxidation at elevated pressures and temperatures was studied by SXRD combined with mass spectrometry using the batch reactor as described above [83, 84].

Previous oxidation experiments have shown that the same surface oxide forms on Rh(111) [45], Rh(100) [51], and Rh(110) [52] surfaces as well as on vicinal Rh surfaces [59, 85]. In addition, the same surface oxide has been found to form on PtRh(100) [86] as well as on Rh nanoparticles [63, 87, 88]. The structure of the trilayer surface oxide is shown in Fig. 3.8a.

Armed with the information from the oxidation studies, the expected reciprocal space for the surface oxide on Rh(111) is shown in Fig. 3.8b. Using a point detector, the scan shown in Fig. 3.8c (left) across the surface oxide allows to detect the presence of the surface oxide combined with online mass spectrometry at a constant temperature of ~240 °C. The results are shown in Fig. 3.8d–g. In Fig. 3.8d the partial pressures of O_2, CO, and CO_2 are shown. Initially, a partial O_2 pressure of 300 mbar was introduced in the reactor, and at time t = 0 s 300 mbar of CO was added to the reactor, starting the CO oxidation and the formation of CO_2. The CO_2 partial pressure is increasing linearly at the same time as the CO and O_2 are decreasing as expected. After around 300 s a sharp increase in the CO_2 partial pressure is observed in conjunction with sharp decreases of the O_2 and CO pressures. The CO_2 production shown in Fig. 3.8e displays only a weak increase until t = 3300 s, when there is a sudden strong increase of the CO_2 production. In Fig. 3.8f, the surface oxide

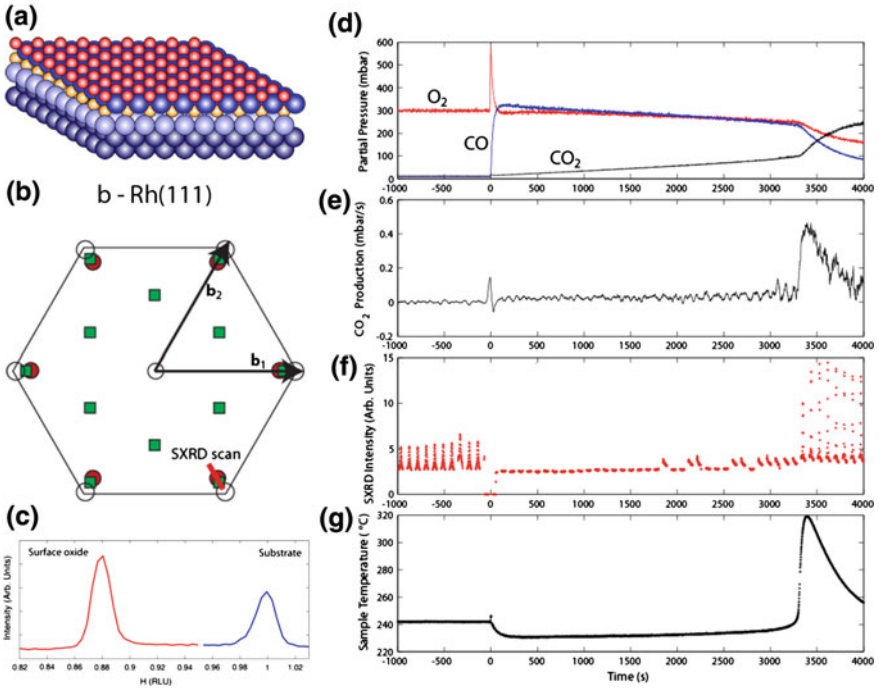

Fig. 3.8 **a** Model of the surface oxide found on all investigated Rh surface orientations, here shown on top of a (111) surface. **b** Reciprocal space map for Rh(111), including the surface oxide as well as the corundum-structured bulk oxide. **c** Line scan along the *red line* in (**b**). **d** partial pressures of O_2, CO, and CO_2. **e** CO_2 production as derived from (**d**). **f** consecutive SXRD scans along the *red line* in (**b**), showing the presence or absence of the surface oxide. **g** sample temperature during the experiment. From [83]

scans, as shown in Fig. 3.8c (left), are shown. When only oxygen is present at this temperature, the surface oxide can be observed, but as soon as the CO is introduced at t = 0 s, the diffraction from the surface oxide disappears. At around t = 3300 s, the surface oxide peak re-appears, in conjunction with the sharp increase in CO_2 production as observed using mass spectrometry. Finally, the sample temperature is shown in Fig. 3.8g, showing that the temperature is decreasing due to the introduction of the CO at t = 0 s, a slow increase until t = 3300 s is observed, at which a strong increase of the sample temperature is detected, indicating heating due to the exothermic nature of the CO-oxidation reaction.

The slow increase of the CO_2 production from t = 0 s to t = 3300 s can be related to a gradual decrease of the CO poisoning of the surface as the gas composition is slowly changed in the reactor. At t = 3300 s, CO suddenly desorbs from the surface and the reaction rapidly becomes mass-transfer-limited (MTL) instead of reaction-limited. In fact, at this point almost all CO in the vicinity of the sample is converted into CO_2 resulting in the sharp peak as observed in the mass spectrometry. The sur-

face oxide is rapidly formed due to the excess oxygen in the vicinity of the sample and the increased temperature. From these measurements, it is not possible to determine the active phase, however, in the case of the PtRh(100) experiments [86], calculations showed that the most active phase was on the border between the Rh surface oxide and the Pt surface underneath. An almost identical experiment was performed for the Rh(100) surface, which showed that the general behavior in terms of surface structure vs. reactivity was the same as for the Rh(111) surface.

3.4.4 Batch Reactor Studies of Nanoparticle Model Systems

A limited number of batch reaction studies on well-defined nanoparticles on single crystal oxide supports combined with surface sensitive X-ray diffraction was performed: In a systematic investigation the nanoparticle size dependence of the CO oxidation turnover frequency was investigated for Au on TiO_2(110) [89]. The highest reactivity was found for a particle diameter of 2.1 nm. In a batch reactor CO oxidation experiment over Pd nanoparticles on MgO(100) with truncated octahedral shape it was observed that carbon is dissolving into the Pd nanoparticles under reaction conditions [90]. At the same time, the produced CO_2 was found to interact with the MgO(100) substrate thereby leading to carbonate formation and a de-activation of the catalyst.

3.5 *Operando* Studies Under Flow Conditions

This section will give a summary of the current state of research of X-ray diffraction experiments using the flow setup described in Sect. 3.2.3. Again, almost all of these studies concern CO oxidation over Pd, Rh, and Pt, but also include a study of methane oxidation over Pd(100).

3.5.1 CO Oxidation Over Pd(100)

As discussed above, there is a debate going on concerning the active phase of Pd(100) during catalytic CO oxidation in O_2 excess. The first use of the flow reactor at ID03 was also directed towards this debate [91, 92].

In [91], a set of measurements is discussed under conditions that were as similar as possible to those used in [93] when a "hyper-active phase" between the CO-poisoned metallic state and the mass-transfer-limited regime was identified. The results were very closely reproduced, with the difference that there were no signs of any extra active phase in between the metallic and mass-transfer-limited regimes. In [93] it was concluded that the most active phase is metallic, covered by adsorbed oxygen,

while the SXRD measurements in [91] clearly showed that the surface is oxidized when the catalytic activity is high.

In a follow-up study the phase diagram of Pd(100) under different reaction conditions was mapped out [92]. The clean sample was exposed to a flow of 50 ml_n/min (1 ml_n is the number of molecules corresponding to 1 ml at standard pressure and temperature) with different CO to O_2 ratios using Ar as a carrier gas at a total pressure of 200 mbar. Simultaneously the surface phase was monitored in situ by SXRD. Using a 2D detector, a common reflection of the PdO surface and bulk oxides was monitored.

The resulting phase diagram is shown in Fig. 3.9. The markers indicate more exactly under which conditions the measurements were done, and whether the surface is metallic (solid symbols) or oxidized (open symbols). To the right of the solid zig-zag line, the surface is metallic and the catalytic activity is relatively low, but increases with temperature. To the left of this line, the activity of the sample is high enough for the measurements to be mass-transfer-limited, and SXRD always reveals an oxide. The nature of this oxide, however, depends on the conditions. The conclusion drawn from these measurements is that, as soon as the activity of the sample is high enough to be mass-transfer-limited, the surface also exposes an oxide. Hence it was argued that the oxide phases must be more active than the metallic surface.

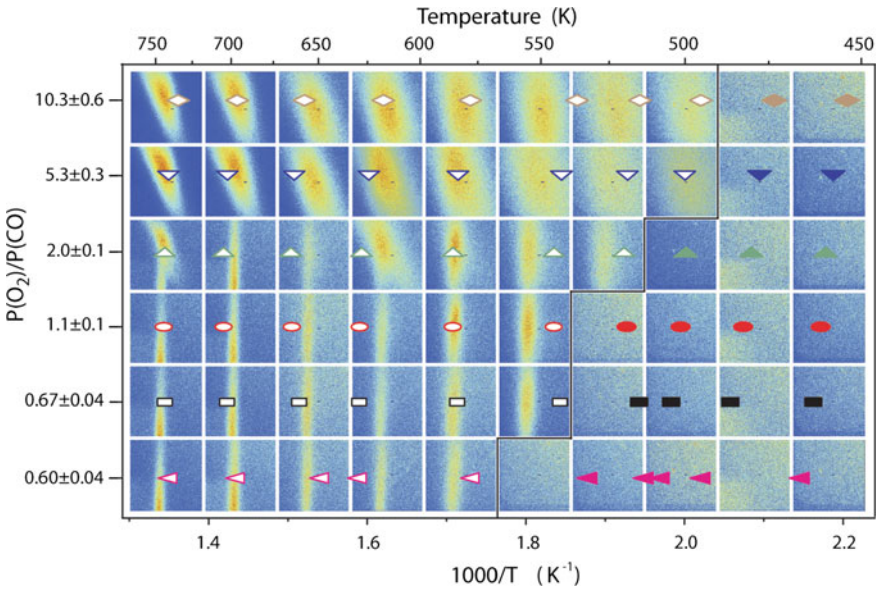

Fig. 3.9 Recorded diffraction signal as a function of the $P(O_2)$:P(CO) ratio and sample temperature. The total gas pressure in the reactor was kept constant at 200 mbar, the partial CO pressure was kept constant at 10 mbar. Oxygen and argon were mixed in the flow to obtain the desired O_2:CO ratio. *Open symbols* denote the presence of an oxide, *filled symbols* denote that the surface was metallic in nature. The *thick black line* indicates the boundary between the metallic and oxidic phases. From [92]

Another interesting phenomenon in catalysis are self-sustained reaction oscillations, which were studied during steady-state CO-oxidation over Pd(100) [94]. At a sample temperature of 447 K and an incoming gas flow of 500 mbar O_2, 25 mbar CO, and 675 mbar Ar, the CO_2 production rate is found to oscillate spontaneously between the MTL and very low activity. As above, *operando* SXRD reveals that the surface is oxidized in the high-activity regime and metallic in the low-activity regime. In addition, the authors have analyzed the width of the diffraction peaks and correlate it to the roughness and number of steps at the surface. In the highly-active, oxidized phase, the surface is found to get rougher and rougher, until the activity switches. In the following low-activity metal phase, the surface smoothens again, until the next switch to high activity. The authors therefore conclude that the oscillations are controlled by the step density at the surface. A high number of steps stabilizes the low-activity metal surface, while a smooth surface more easily oxidizes into the high-activity phase.

3.5.2 CO Oxidation Over Rh(111)

Also CO oxidation over Rh(111) has been studied in the flow reactor [95, 96]. In flows of different gas mixtures, around a stoichiometric mixture of CO and O_2, the Rh(111) sample was heated and cooled while the catalytic activity and the presence of the surface oxide were monitored by mass spectrometry and SXRD, respectively. The activity follows the sample temperature smoothly until a sample temperature of between 200 and 250 °C. At this temperature, the experiments performed in an excess of O_2 show a sudden jump into a highly active mass-transfer-limited regime, while in a CO-rich gas flow, the activity continues to increase smoothly with the temperature. The SXRD measurements reveal that the switch to the mass-transfer-limited regime (in O_2 excess) coincides with the appearance of a surface oxide. The surface-oxide signal does not grow to full strength immediately, which suggests a combination of low coverage and small domains.

3.5.3 CO Oxidation Over Stepped Surfaces

The above discussion makes it very clear that surfaces change drastically with the exposure to reaction gas mixtures. This is not less true for stepped surfaces, which are used to investigate the effect of defects on catalytic reactions [97, 98]. Since CTRs are always perpendicular to the surface, the appearance of new facets is revealed by the appearance of CTRs in new directions. Figure 3.10 shows a map of reciprocal space around the Pt(977) Bragg reflections at $(H, K, L) = (16, 0, 5)$ and $(18, 0, 28)$ [97]. Vertically from these Bragg reflections there are two CTRs revealing the overall (553) orientation of the surface. In addition, there is one CTR connecting the Bragg reflections, and hence leaning slightly. This CTR is perpendicular to the (111) facets

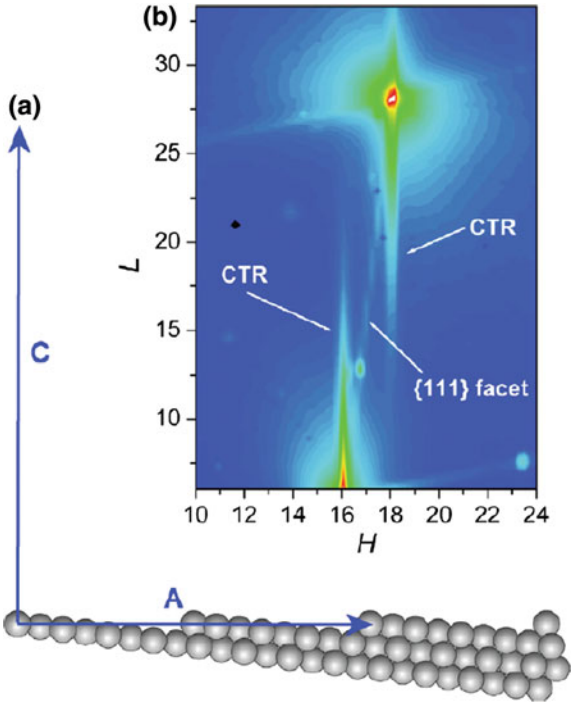

Fig. 3.10 **a** Side view of the (977) surface and representation of the A and C vectors in direct space. C is perpendicular to the 997 planes and A has a length twice the step separation. **b** Diffracted intensities in a portion of the plane (H,L) at K = 0 in reciprocal space. The H and L axes are parallel to vectors A and C respectively. The intense *red spot* at (H, L) = (18, 28) arises from a Bragg reflection from the bulk of the crystal. The diffuse intensity streak emanating from the Bragg reflection, parallel to the L axis, is a crystal truncation rod (CTR) of the 977 surface plane. At (H, L) = (16, 5) there is another Bragg reflection which tail is visible in the lower part of the figure. Again, its associated diffraction rod from the stepped surface parallel to the L axis is noticeable. In addition, an inclined diffuse intensity line connecting the two bulk Bragg reflections is visible. It corresponds to a diffracted rod from (111) surface planes indicative of the existence of surface (111)s facets. From [97]

that make up the terraces between the steps. For a perfect (977) surface, the (111) CTR should cancel out, but there are always small variations in the terrace size, such that for the clean surface a combination of (997) and (111) CTRs was found. During this study, the evolution of the (111) and (997) facets is followed by line scans revealing the intensity of the corresponding CTRs, while the reaction gas mixture is varied. In a stoichiometric mixture of CO and O_2 the (977) facet becomes more visible, while excess of either CO or O_2 causes rearrangements of the surface into larger (111) facets. In order for the macroscopic surface orientation to remain in the (977) direction, the growth of (111) facets must be accompanied by step bunching, but the structure of the areas where the steps bunch together is unclear from the present study.

Similar observations were made for the Rh(553) surface [98]. Analogous to the Pt(977) case above, in close to stoichiometric gas mixtures with slight CO excess, the presence of (553) and (111) CTRs is reported, while larger excess of CO or excess of O_2 both results in faceting of the surface. Here, the 2D maps make it possible to find out what happens in the areas with increased step intensities. In CO excess the formation of a CTR in the (110) direction is found, while O_2 excess results in new (331) rods, showing that facets with the corresponding orientations are formed. In addition, at large excess of O_2, there is an extra rod in the (111) direction, showing the formation of the surface oxide on the enlarged (111) terraces.

3.5.4 Methane Oxidation Over Pd(100)

Another example of the use of the 2D detector to identify the active phase of a Pd(100) model catalyst is methane (CH_4) oxidation [99]. In relatively low pressures ($P(CH_4)$:$P(O_2)$ = 0.1:0.5 mbar), the surface is always inactive in the oxide phase and the activity starts when the temperature is high enough in order to transform the surface into a metallic state. The 2D diffraction map of the oxide, both in the beginning and in the end, shows a vertical extended reflection, which is indicative of an ultrathin surface oxide.

At higher pressure ($P(CH_4)$:$P(O_2)$ = 6:16 mbar), however, there is an active regime at lower temperatures where the surface is still oxidized, but the activity drops before it increases again when the surface turns metallic. As the temperature increases, the detector images evolve from a vertical line with rather smooth intensity through a vertical line with intensity more and more concentrated in one spot, to a strongly leaning line with a very strong maximum. This reflects the development of the oxide from a surface oxide through an epitaxial bulk oxide into a polycrystalline oxide structure. Theoretical calculations have predicted that an oxide growing on Pd(100) will expose PdO(101)-oriented surface facets, while PdO on its own (or a thick enough film on Pd(100)) will expose (100) oriented facets. Hence the following conclusions can be drawn from the measurements: They show the transformation from a surface oxide to an epitaxial oxide exposing (101) facets, and finally the oxide gets thick enough to lose its registry with the substrate, becomes polycrystalline and exposes (100) facets. This would also explain the activity variations, as PdO(101) exposes undercoordinated Pd atoms that are predicted to be the active sites, while PdO(100) does not expose such sites.

3.5.5 The Use of Large 2D Detectors in Combination with High X-ray Photon Energies

Finally, surface-sensitive X-ray diffraction is right now going through a revolution with the use of large 2D detectors. As demonstrated in [100, 101], the combination of high-energy X-rays (70–90 keV) and a large 2D detector makes it possible to col-

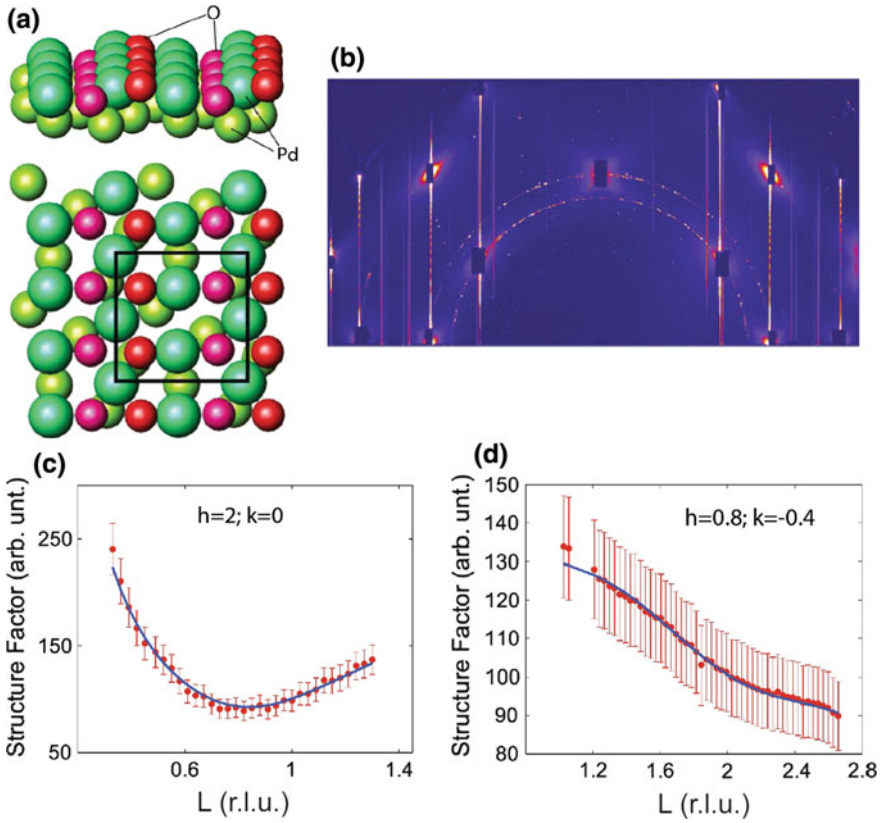

Fig. 3.11 In situ HESXRD data from the surface oxide on Pd(100) measured during CO oxidation in a flow of 6 Torr CO and 3 Torr O_2 at a sample temperature of 600 K. **a** Top and side view of the relevant oxygen-induced ($\sqrt{5} \times \sqrt{5}$)R27° surface oxide structure. The structure is an O-Pd-O trilayer corresponding to one PdO(101) plane. **b** All images collected during the rotational scan combined into a single image, in which the CTRs and superlattice rods can be directly seen. **c** and **d** Extracted (*dots*) CTRs and superlattice rods from the rotational images as seen in (**b**), and calculated structure factors (*full lines*). From [100]

lect from a single-crystal surface a large range of diffraction angles with a stationary detector, and through a simple rotation of the sample, a 3D map of the reciprocal space is acquired in about 15 min. The strength of the combination of high photon energies with 2D detectors for the investigation of epitaxial nanoparticle model catalyst systems was discussed in Sect. 3.3.3. As illustrated by Fig. 3.11 for the case of the Pd(100) surface during CO oxidation, the resulting data can be represented in several different ways in order to directly show the presence of different CTRs and superstructure rods, and to extract data for quantitative surface-structure determinations. These measurements are superior to conventional SXRD in the sense that they speed up the measurements by several orders of magnitude. In conventional SXRD it

is practically impossible to map out the reciprocal space in 3D, which means that it is very easy to miss structures that are not expected. This is not the case with the large 2D detector. The large detector is also able to explore a higher fraction of the reciprocal space without rotating the sample, which improves the use of time-resolved measurements. This is especially true for the combination with high-energy X-rays, since the flatter Ewald sphere makes it easier to select an interesting area to cover. Future experiments using high energies will enable the investigation of nanoparticle model catalysts under flow reaction conditions [102], and the combination with other techniques such as laser induced fluorescence or Fourier transform infrared spectroscopy will shed new light on the open questions concerning the most active phase of a catalyst under flow reaction conditions.

References

1. R. Feidenhans'l, Surf. Sci. Rep. **10**, 105 (1989)
2. H. Dosch, *Critical phenomena at surfaces and interfaces*, Springer Tracts in Modern Physics. (Springer, Berlin, 1992), p. 126
3. I.K. Robinson, D.J. Tweet, Rep. Prog. Phys. **55**, 599 (1992)
4. A. Stierle, E. Vlieg, *Surface Sensitive X-ray Diffraction Methods in Modern Diffraction Methods*, ed. by E.J. Mittemeijer, U. Welzel. (Wiley VHC Weinheim, 2013)
5. E. Vlieg, J. Appl. Cryst. **30**, 532 (1997)
6. A. Stierle, H.-D. Carstanjen, W. Hofmann, O.H. Seeck, *Structural and Chemical Characterization on the Nanoscale in Nanoelectronics and Information Technology, edited by R* (Waser, Wiley VCH Weinheim, 2012)
7. N. Kasper, A. Stierle, P. Nolte, Y. Jin-Phillipp, T. Wagner, D.G. de Oteyza, H. Dosch, Surf. Sci. **600**, 2860 (2006)
8. U. Pietsch, V. Holy, T. Baumbach, *High-Resolution X-ray Scattering* (Springer, Berlin, 2004)
9. G. Renaud, R. Lazzari, F. Leroy, Surf. Sci. Rep. **64**, 255 (2009)
10. http://www.lightsources.org/
11. B.E. Warren, *X-ray Diffraction* (Dover Publications Inc, Mineola, 1990)
12. M. Lohmeier, E. Vlieg, J. Appl. Cryst. **26**, 706 (1993)
13. C.M. Schlepütz, R. Herger, P.R. Willmott, B.D. Patterson, O. Bunk, Ch. Brönnimann, B. Henrich, G. Hülsen, E.F. Eikenberry, Acta Cryst. **A61**, 418 (2005)
14. J. Drnec, T. Zhou, S. Pintea, W. Onderwaater, E. Vlieg, G. Renaud, R. Felicia, J. Appl. Cryst. **47**, 365 (2014)
15. D.K. Saldin, V.L. Shneerson, J. Phys.: Condens. Matter **20**, 304208 (2008)
16. L.G. Parratt, Phys. Rev. **95**, 359 (1954)
17. L. Nèvot, P. Croce, Revue de Physique Appl. **15**, 761 (1980)
18. W. Weber, B. Lengeler, Phys. Rev. B Rapid Comm. **46**, 7953 (1992)
19. S.K. Sinha, E.B. Sirota, S. Garoff, H.B. Stanley, Phys. Rev. B **38**, 2297 (1988)
20. J. Als-Nielsen, D. McMorrow, *Elements of Modern X-ray Physics* (Wiley, 2011)
21. O. Balmes, R. van Rijn, D. Wermeille, A. Resta, L. Petit, H. Isern, T. Dufrane, R. Felici, Catal. Today **145**, 220 (2009)
22. P. Bernard, K. Peters, J. Alvarez, S. Ferrer, Rev. Sci. Instrum. **70**, 1478 (1999)
23. R. van Rijn et al., Rev. Sci. Instrum. **81**, 014101 (2010)
24. M.-C. Saint-Lager, A. Bailly, P. Dolle, R. Baudoing-Savois, P. Taunier, S. Garaude, S. Cuccaro, S. Douillet, O. Geaymond, G. Perroux, O. Tissot, J.-S. Micha, O. Ulrich, F. Rieutord, Rev. Sci. Instrum. **78**, 083902 (2007)
25. A.K. Santra, D.W. Goodman, J. Phys.: Condens. Matter. **14**, R31 (2002)

26. H. Over, Y.D. Kim, A.P. Seitsonen, S. Wendt, E. Lundgren, M. Schmid, P. Varga, A. Morgante, G. Ertl, Science **287**, 1474 (2000)
27. A. Nagy, G. Mestl, Appl. Cat. A: General **188**, 337 (1999)
28. V.I. Bukhtiyarov, M. Hvecker, V.V. Kaichev, A. Knop-Gericke, R.W. Mayer, R. Schlögl, Phys. Rev. B **67**, 235422 (2003)
29. G. Rovida, F. Pratesi, M. Maglietta, E. Ferroni, Surf. Sci. **43**, 230 (1974)
30. C.I. Carlisle, D.A. King, M.-L. Bocquet, J. Cerda, P. Sautet, Phys. Rev. Lett. **84**, 3899 (2000)
31. W.-X. Li, C. Stampfl, M. Scheffler, Phys. Rev. B **67**, 045408 (2003)
32. M. Todorova, W.X. Li, M.V. Ganduglia-Pirovano, C. Stampfl, K. Reuter, M. Scheffler, Phys. Rev. Lett. **89**, 096103 (2002)
33. A. Michaelides, K. Reuter, M. Scheffler, J. Vac. Sci. Technol. A **23**, 1487 (2005)
34. M. Schmid, A. Reicho, A. Stierle, I. Costina, J. Klikovits, P. Kostelnik, O. Dubay, G. Kresse, J. Gustafson, E. Lundgren, J.N. Andersen, H. Dosch, P. Varga, Phys. Rev. Lett. **96**, 146102-1-4 (2006)
35. J. Schnadt, A. Michaelides, J. Knudsen, R.T. Vang, K. Reuter, E. Lægsgaard, M. Scheffler, F. Besenbacher, Phys. Rev. Lett. **96**, 146101 (2006)
36. A. Reicho, A. Stierle, I. Costina, H. Dosch, Surf. Sci. **601** L19L23 (2007)
37. A. Stierle, I. Costina, S. Kumaragurubaran, H. Dosch, J. Phys. Chem. C **111**, 10998 (2007)
38. M. Rocca, L. Savio, L. Vattuone, U. Burghaus, V. Palomba, N. Novelli, F. Buatier de Mongeot, U. Valbusa, R. Gunnella, G. Comelli, A. Baraldi, S. Lizzit, G. Paolucci, Phys. Rev. B **61**, 213 (2000)
39. H. Iddir, D.D. Fong, P. Zapo, P.H. Fuoss, L.A. Curtiss, G.-W. Zhou, J.A. Eastman, Phys. Rev. B **76**, 241404 R (2007)
40. E. Lundgren, G. Kresse, C. Klein, M. Borg, J.N. Andersen, M. De Santis, Y. Gauthier, C. Konvicka, M. Schmid, P. Varga, Phys. Rev. Lett. **88**, 246103 (2002)
41. P. Kostelnik, N. Seriani, G. Kresse, A. Mikkelsen, E. Lundgren, V. Blum, T. Sikola, P. Varga, M. Schmid, Surf. Sci. **601**, 1574 (2007)
42. B.L.M. Hendriksen, S.C. Bobaru, J.W.M. Frenken, Surf. Sci. **552**, 229 (2004)
43. J. Rogal, K. Reuter, M. Scheffler, Phys. Rev. Lett. **98**, 046101 (2007)
44. M.S. Chen, Y. Cai, Z. Yan, K.K. Gath, S. Axnanda, D.W. Goodman, Surf. Sci. **601**, 5326 (2007)
45. J. Gustafson, A. Mikkelsen, M. Borg, E. Lundgren, L. Köhler, G. Kresse, M. Schmid, P. Varga, J. Yuhara, X. Torrelles, C. Quiros, J.N. Andersen, Phys. Rev. Lett. **92**, 126102 (2004)
46. E. Lundgren, J. Gustafson, A. Mikkelsen, J.N. Andersen, A. Stierle, H. Dosch, M. Todorova, J. Rogal, K. Reuter, M. Scheffler, Phys. Rev. Lett. **92**, 046101 (2004)
47. A. Stierle, N. Kasper, H. Dosch, E. Lundgren, J. Gustafson, A. Mikkelsen, J.N. Andersen, J. Chem. Phys. **122**, 044706 (2005)
48. N. Kasper, P. Nolte, A. Stierle, J. Phys. Chem. C **116**(40), 21459 (2012)
49. R. Westerström, C.J. Weststrate, J. Gustafson, A. Mikkelsen, J. Schnadt, J.N. Andersen, E. Lundgren, N. Seriani, F. Mittendorfer, G. Kresse, A. Stierle, Phys. Rev. B **80**, 125431 (2009)
50. C.W. Tucker, J. Appl. Phys. **37**, 3013 (1966)
51. J. Gustafson, A. Mikkelsen, M. Borg, J.N. Andersen, E. Lundgren, C. Klein, W. Hofer, M. Schmid, P. Varga, L. Köhler, G. Kresse, N. Kasper, A. Stierle, H. Dosch, Phys. Rev. B **71**, 115442 (2005)
52. C. Dri, C. Africh, F. Esch, G. Comelli, O. Dubay, L. Köhler, F. Mittendorfer, G. Kresse, P. Dudin, M. Kiskinova, J. Chem. Phys. **125**, 094701 (2006)
53. W.X. Li, L. österlund, E.K. Vestergaard, R.T. Vang, J. Matthiesen, T.M. Pedersen, E. Lægsgaard, B. Hammer, F. Besenbacher, Phys. Rev. Lett. **93**, 146104 (2004)
54. M.D. Ackermann, T.M. Pedersen, B.L.M. Hendriksen, O. Robach, S.C. Bobaru, I. Popa, C. Quiros, H. Kim, B. Hammer, S. Ferrer, J.W.M. Frenken, Phys. Rev. Lett. **95**, 255505 (2005)
55. C. Ellinger, A. Stierle, I.K. Robinson, A. Nefedov, H. Dosch, J. Phys. Cond. Mat. **20**, 184013 (2008)
56. Y.B. He, A. Stierle, W.X. Li, A. Farkas, N. Kasper, H. Over, J. Phys. Chem. C **112**, 11946 (2008)

57. R. Westerström, J. Gustafson, A. Resta, A. Mikkelsen, J.N. Andersen, E. Lundgren, N. Seriani, F. Mittendorfer, M. Schmid, J. Klikovits, P. Varga, M.D. Ackermann, J.W.M. Frenken, N. Kasper, A. Stierle, Phys. Rev. B **76**, 155410 (2007)
58. A. Vlad, A. Stierle, R. Westerström, S. Blomberg, A. Mikkelsen, E. Lundgren, Phys. Rev. B **86**, 035407 (2012)
59. J. Gustafson, A. Resta, A. Mikkelsen, R. Westerström, J.N. Andersen, E. Lundgren, J. Weissenrieder, M. Schmid, P. Varga, N. Kasper, X. Torrelles, S. Ferrer, F. Mittendorfer, G. Kresse, Phys. Rev. B **74**, 035401 (2006)
60. M.A. Newton, C. Belver-Coldeira, A. Martinez-Arias, M. Fernandez-Garcia, Nat. Mat. **6**, 528 (2007)
61. C.R. Henry, Surf. Sci. Rep. **31**, 231 (1998)
62. P. Nolte, A. Stierle, N. Kasper, N. Jeutter, H. Dosch, Nano Lett. **11**, 4697 (2011)
63. P. Nolte, A. Stierle, N.Y. Jin-Phillipp, N. Kasper, T.U. Schulli, H. Dosch, Science **321**, 1654–1658 (2008)
64. F. Mittendorfer, N. Seriani, O. Dubay, G. Kresse, Phys. Rev. B **76**, 233413 (2007)
65. P. Nolte, A. Stierle, N. Kasper, N.Y. Jin-Phillipp, H. Reichert, A. Rühm, J. Okasinski, H. Dosch, S. Schöder, Phys. Rev. B **77**, 115444 (2008)
66. P. Müller, U. Hejral, U. Rütt, A. Stierle, Phys. Chem. Chem. Phys. **16**, 13866 (2014)
67. U. Hejral, A. Vlad, P. Nolte, A. Stierle, J. Phys. Chem. C **117**(39), 19955 (2013)
68. K.F. Peters, C.J. Walker, P. Steadman, O. Robach, H. Isern, S. Ferrer, Phys. Rev. Lett. **86**, 5325 (2001)
69. M.C. Saint-Lager, Y. Jugnet, P. Dolle, L. Piccolo, R. Baudoing-Savois, J.C. Bertolini, A. Bailly, O. Robach, C. Walker, S. Ferrer, Surf. Sci. **587**, 229 (2005)
70. M.D. Ackermann, T.M. Pedersen, B.L.M. Hendriksen, O. Robach, S.C. Bobaru, I. Popa, C. Quiros, H. Kim, B. Hammer, S. Ferrer, J.W.M. Frenken, Phys. Rev. Lett. **95**, 255505 (2005)
71. Y.B. He, M. Knapp, E. Lundgren, H. Over, J. Phys. Chem. B **109**, 21825 (2005)
72. H. Over, O. Balmes, E. Lundgren, Surf. Sci. **603**, 298 (2009)
73. H. Over, O. Balmes, E. Lundgren, Catal. Today **145**, 236 (2009)
74. S. Zweidinger, D. Crihan, M. Knapp, J.P. Hofmann, A.P. Seitsonen, C.J. Westrate, E. Lundgren, J.N. Andersen, H. Over, J. Phys. Chem. C **112**, 9966 (2008)
75. H. Deacon, US Patent (1875) 0165802
76. K. Iwanaga, K. Seki, T. Hibi, K. Issoh, T. Suzuta, M. Nakada, Y. Mori, T. Abe, The development of improved hydrogen chloride oxidation process. Sumitomo Kagaku **I**, 1 (2004)
77. D. Crihan, M. Knapp, S. Zweidinger, E. Lundgren, C.J. Weststrate, J.N. Andersen, A.P. Seitsonen, H. Over, Angew. Chem. Int. Ed. **47**, 2131 (2008)
78. N. López, J. Gmez-Segura, R.P. Marn, J. Prez-Ramrez, J. Catal. **255**, 29 (2008)
79. S. Zweidinger, J.P. Hofmann, O. Balmes, E. Lundgren, H. Over, J. Catal. **272**, 169 (2010)
80. M.V. Ganduglia-Pirovano, M. Scheffler, A. Baraldi, S. Lizzit, G. Comelli, G. Paolucci, R. Rosei, Phys. Rev. B **63**, 205415 (2001)
81. A. Baraldi, J. Phys. Condens. Matter **20**, 093001 (2008)
82. C.H.F. Peden, D.W. Goodman, D.S. Blair, P.J. Berlowitz, G.B. Fischer, S.H. Oh, J. Phys. Chem. **92**, 1563 (1988)
83. J. Gustafson, R. Westerström, A. Mikkelsen, X. Torrelles, O. Balmes, J.N. Andersen, C.J. Baddeley, E. Lundgren, Phys. Rev. B **78**, 045423 (2008)
84. J. Gustafson, R. Westerström, A. Mikkelsen, A. Resta, J.N. Andersen, X. Torrelles, O. Balmes, M. Schmid, P. Varga, B. Hammer, G. Kresse, C.J. Baddeley, E. Lundgren, Catal. Today **145**, 227 (2009)
85. J. Klikovits, M. Schmid, L.R. Merte, P, Varga, R. Westerström, A. Resta, J.N. Andersen, J. Gustafson, A. Mikkelsen, E. Lundgren, F. Mittendorfer, G. Kresse, Phys. Rev. Lett. **101**, 266104 (2008)
86. R. Westerström, J.G. Wang, M. Ackermann, J. Gustafson, A. Resta, A. Mikkelsen, J.N. Andersen, E. Lundgren, O. Balmes, X. Torrelles, J.W.M. Frenken, B. Hammer, J. Phys. Condens. Matter **20**, 184018 (2008)
87. G. Rupprechter, K. Hayek, H. Hofmeister, J. Catal. **173**, 409 (1998)

88. S. Blomberg, R. Westerström, N.M. Martin, E. Lundgren, J.N. Andersen, M.E. Messing, J. Gustafson, Surf. Sci. **628**, 153 (2014)
89. I. Laoufi, M.-C. Saint-Lager, R. Lazzari, J. Jupille, O. Robach, S. Garaudee, G. Cabailh, P. Dolle, H. Cruguel, A. Bailly, J. Phys. Chem. C **4673**, 115 (2011)
90. P. Nolte, A. Stierle, O. Balmes, V. Srot, P.A. van Aken, L.P.H. Jeurgens, H. Dosch, Catal. Today **145**, 243 (2009)
91. R. van Rijn, O. Balmes, R. Felici, J. Gustafson, D. Wermeille, R. Westerström, E. Lundgren, J.W.M. Frenken, J. Phys. Chem. C **114**, 6875–6876 (2010)
92. R. van Rijn, O. Balmes, A. Resta, D. Wermeille, R. Westerström, J. Gustafson, R. Felici, E. Lundgren, J.W.M. Frenken, Phys. Chem. Chem. Phys. **13**, 13167–13171 (2011)
93. F. Gao, Y. Wang, Y. Cai, D.W. Goodman, J. Phys. Chem. C **113**, 174–181 (2009)
94. B.L.M. Hendriksen, M.D. Ackermann, R. van Rijn, D. Stoltz, I. Popa, O. Balmes, A. Resta, D. Wermeille, R. Felici, S. Ferrer, J.W.M. Frenken, Nat. Chem. **2**, 730–734 (2010)
95. J. Gustafson, R. Westerström, O. Balmes, A. Resta, R. van Rijn, X. Torrelles, C.T. Herbschleb, J.W.M. Frenken, E. Lundgren, J. Phys. Chem. C **114**, 4580–4583 (2010)
96. J. Gustafson, R. Westerström, O. Balmes, A. Resta, R. van Rijn, X. Torrelles, C.T. Herbschleb, J.W.M. Frenken, E. Lundgren, J. Phys. Chem. C **114**, 22372–22373 (2010)
97. O. Balmes, G. Prevot, X. Torrelles, E. Lundgren, S. Ferrer, J. Catal. **309**, 33–37 (2014)
98. C. Zhang, E. Lundgren, P.-A. Carlsson, O. Balmes, A. Hellman, L.R. Merte, M. Shipilin, W. Onderwaater, J. Gustafson, J. Phys. Chem. C **119**, 11646–11652 (2015)
99. A. Hellman, A. Resta, N.M. Martin, J. Gustafson, A. Trinchero, P.-A. Carlsson, O. Balmes, R. Felici, R. van Rijn, J.W.M. Frenken, J.N. Andersen, E. Lundgren, H. Grönbeck, J. Phys. Chem. Lett. **3**, 678–682 (2012)
100. J. Gustafson, M. Shipilin, C. Zhang, A. Stierle, U. Hejral, U. Ruett, O. Gutowski, P.-A. Carlsson, M. Skoglundh, E. Lundgren, Science **343**, 758–761 (2014)
101. M. Shipilin, U. Hejral, E. Lundgren, L.R. Merte, C. Zhang, A. Stierle, U. Ruett, O. Gutowski, M. Skoglundh, P.-A. Carlsson, J. Gustafson, Surf. Sci. **630**, 229–235 (2014)
102. U. Hejral, P. Müller, O. Balmes, D. Pontoni, A. Stierle, Nat. Comm. **7**, 10964 (2016)